



Cite this: *J. Mater. Chem. C*, 2015, **3**, 12068

Transition metal doped pyrite (FeS₂) thin films: structural properties and evaluation of optical band gap energies†

Sadia Khalid,^{abc} Mohammad Azad Malik,^{*ad} David J. Lewis,^{ad} Punarja Kevin,^d Ejaz Ahmed,^b Yaqoob Khan^c and Paul O'Brien^{ad}

Iron pyrite (FeS₂) is a semiconductor comprised of earth-abundant elements and has the potential to be a low cost photovoltaic material with comparatively low toxicity. The properties of transition metal doped iron pyrite thin films (M_xFe_{1-x}S₂ where M = Co, Ni, Cu, or Zn) deposited by aerosol-assisted chemical vapour deposition (AACVD) on various substrates including glass, (100) silicon and indium tin oxide (ITO) have been studied. Changes in the cubic lattice parameter as well as peak broadening on doping were observed by powder X-ray diffraction (p-XRD) measurements. The structural properties of the transition metal doped pyrite (M_xFe_{1-x}S₂) depend strongly on the transition metal dopant used and preferred orientation in all films was found to be along the (200) plane. The influence of transition metal doping on the structure and phase transformation was significant in copper doped pyrite thin films. The height-profiling of M_xFe_{1-x}S₂ films with atomic force microscopy (AFM) displayed smooth surfaces with uniform distribution of particles. Optical studies revealed that there is increment in the bandgap of M_xFe_{1-x}S₂ thin films which is supported by previous work. There may be contribution from oxidation of the doped pyrite surface in band gap enhancement observed by X-ray photoelectron spectroscopy (XPS). These findings may be important to improve doped pyrite layers for photovoltaic devices.

Received 11th October 2015,
Accepted 30th October 2015

DOI: 10.1039/c5tc03275j

www.rsc.org/MaterialsC

1. Introduction

Transition metal sulfides have attractive optical properties for photovoltaics, with high extinction coefficients and band gaps commensurate with the solar photon flux. Iron pyrite (or cubic iron disulfide), β-FeS₂ ($E_g = 0.95$ eV; absorption coefficient, $\alpha > 10^5$ cm⁻¹ at $h\nu > 1.3$ – 1.4 eV, is potentially the most important transition metal sulfide for sustainable energy applications. Due to the inexpensive nature of its constituent elements, pyrite could potentially expand the opportunity for wide-scale deployment of photovoltaic modules.¹ The material is also relatively non-toxic compared with other semiconducting materials used in photovoltaic applications. Additionally, pyrite has also found numerous applications in optoelectronic devices,^{2,3} energy

conversion/storage devices,^{4,5} agriculture,⁶ biomedical applications⁷ and extreme pressure additives in formulated oils.⁸ Organohalide lead(II) perovskites such as methylammonium lead(II) iodide (CH₃NH₃PbI₃)⁹ have also emerged as light-harvesting semiconductors for thin film solar cells along with copper indium gallium selenide (CIGS),¹⁰ copper zinc tin sulfide (CZTS)¹¹ and quantum dot sensitised solar cells such as those based on nanocrystalline cadmium selenide (CdSe).¹²

The ternary chalcogenides of chalcopyrite type structure (CuInS₂, CuGaS₂, CuInSe₂ or CuGaSe₂)^{13,14} are excellent solar harvesters and highly efficient counter electrodes in dye/quantum dot sensitized solar cells.¹⁵ However, many of these materials suffer from potential barriers to mass commercialisation either from toxicity issues (heavy metals such as lead and cadmium), stability to humidity or from the scarcity of one or more of their constituent elements in the Earth's crust.

Pyrite-based photovoltaic devices display low power conversion efficiencies (only up to ca. 3%) that are generally attributed to surface defects which cause low open circuit voltages (V_{OC}).¹⁶ Different strategies have been employed for improvement of photovoltaic properties of pyrite¹⁷ including bandgap tuning by doping/alloying¹⁸ and by fabrication of pyrite composites.⁸ Sun *et al.* have investigated from first principles density-functional theory (DFT) calculations that the band gap of pyrite can be

^a School of Materials, The University of Manchester, Oxford Road, Manchester, M13 9PL, UK. E-mail: azad.malik@manchester.ac.uk; Fax: +44 (0)161 275 4616; Tel: +44 (0)161 275 4652

^b Department of Physics, Bahauddin Zakariya University, Multan 60800, Pakistan

^c Nano Science & Catalysis Division, National Centre for Physics, Shahdara Valley Road Quaid-i-Azam University Campus, Islamabad 45320, Pakistan

^d School of Chemistry, The University of Manchester, Oxford Road, Manchester, M13 9PL, UK

† Electronic supplementary information (ESI) available: Tauc plots and photoluminescence spectra. See DOI: 10.1039/c5tc03275j



increased slightly by cation substitution with ruthenium (Ru) or osmium (Os) to form materials $\text{Fe}_{1-x}\text{Ru}_x\text{S}_2$ and $\text{Fe}_{1-x}\text{Os}_x\text{S}_2$ but their incorporation into pyrite is limited by the large positive enthalpy of mixing.¹⁹ Engineering the band gap of pyrite materials by doping potentially makes it possible to produce pyrite photovoltaic devices which utilise architectures based on combinations of wide to narrow bandgaps to increase the power conversion efficiency by capturing more of the solar spectrum.

We have reported the synthesis of single source precursors and their use to deposit semiconductor thin films or nanoparticles.^{20–27} Recently we reported the aerosol-assisted chemical vapour deposition (AACVD) of a range of materials pertinent to photovoltaic applications, including the organic lead halide perovskite methylammonium lead(II) bromide²⁸ copper sulphide, copper indium sulphide,¹⁴ and tin sulphide,^{29,30} iron selenide³¹ and, significantly, transition metal doped iron sulphide.³² In this paper we report on structural and surface properties of transition metal ($\text{M} = \text{Co}, \text{Ni}, \text{Cu}, \text{Zn}$) doped pyrite ($\text{M}_x\text{Fe}_{1-x}\text{S}_2$) thin films as well as fully evaluating the effect of doping on the optical band gap energy.

2. Experimental

2.1. Synthesis of precursors (1–5) and deposition of ($\text{M}_x\text{Fe}_{1-x}\text{S}_2$ where $\text{M} = \text{Co}, \text{Ni}, \text{Cu}, \text{or Zn}$) thin films

Transition metal diethyldithiocarbamate complexes (1), $[\text{Co}(\text{S}_2\text{CNET}_2)_3]$ (2), $[\text{Ni}(\text{S}_2\text{CNET}_2)_2]$ (3), $[\text{Cu}(\text{S}_2\text{CNET}_2)_2]$ (4) and $[\text{Zn}(\text{S}_2\text{CNET}_2)_2]$ (5) were prepared and used to deposit $\text{M}_x\text{Fe}_{1-x}\text{S}_2$ (where $\text{M} = \text{Co}, \text{Ni}, \text{Cu}, \text{Zn}$) thin films by AACVD as described previously³² onto glass, Si(100) and ITO-coated glass. In a typical deposition, 0.3 g (0.6 mmol) of the iron precursor (1) and varying concentration of the dopant precursors (2–5) (0.05 mol%, 0.1 mol%, 0.15 mol%, 0.20 mol%, 0.25 mol%, 0.30 mol%) were used.

2.2. Deposition of thin films

Thin films were deposited using AACVD. Glass, silicon or ITO coated glass slides (1×2 cm) were used as substrates for the deposition. Substrates were thoroughly cleaned and sonicated in acetone for 30 minutes to remove any possible contamination. In a typical deposition experiment, precursor complex (or a suitable combination of precursors) was dissolved in 15 mL toluene taken in a two-necked 100 mL round-bottom flask. The flask was then connected with an argon gas inlet which passed through the solution and carried the aerosols generated by a PIFCO ultrasonic humidifier to the reactor tube connected to other neck of the flask and placed in a Carbolite furnace. The argon flow rate was controlled at 180 sccm by a Platon flow gauge. Thermolysis of the precursor at the hot substrate surface due to thermally induced reactions led to deposition onto the substrates.

2.3. Characterization of thin films

p-XRD studies were performed on an Xpert diffractometer using $\text{Cu-K}\alpha$ radiation ($\lambda = 1.5406$ Å). The samples were mounted flat and scanned between $2\theta = 25^\circ$ and 65° with a step size of 0.02° . AFM was carried using a Bruker multimode

8 atomic force microscope operating in Peakforce QNM mode, using a silicon nitride tip. Raman spectroscopy was performed using a Renishaw 1000 microscope system equipped with a $50\times$ objective, with solid-state laser excitation (514.5 nm, 25% power). The incident light was linearly polarised in the sample plane with scattered light left un-analysed for collection by the air cooled CCD. XPS spectra were recorded using a Kratos Axis Ultra spectrometer. Optical measurements were performed at room temperature using Perkin Elmer Lambda 950 UV/Vis/NIR spectrophotometer in the wavelength range 200–1200 nm. Photoluminescence spectra were measured using an Edinburgh Instruments FLS920 spectrofluorimeter. Band gap energies were calculated from the obtained absorbance spectra.

3. Results and discussion

3.1. Optical band gaps of doped pyrite films

The optical band gap of pyrite thin films deposited at 350°C using precursor (1) by AACVD were determined from absorbance measurements by Tauc plots (Fig. S1–S4, ESI†). The indirect bandgap for pyrite thin films was calculated as $E_g = 0.92$ eV (Fig. S5, ESI†) which is in accordance with the previously reported bandgap value ($E_g \approx 0.95$ eV). Band gap studies revealed the improvement in band gap values as well as in absorption coefficient in transition metal doped pyrite ($\text{M}_x\text{Fe}_{1-x}\text{S}_2$) thin films. The optical spectra of as-deposited films using precursors (1) and varying concentration of the dopant precursors of (2–5) (0.05 mol%, 0.1 mol%, 0.15 mol%, 0.20 mol%, 0.25 mol%, 0.30 mol%) were studied by UV-Vis-NIR spectroscopy. Absorption spectra reveal shifts in the absorption edges by transition metal doping. The energy of the optical bandgap (E_g) was estimated using Tauc plots by plotting energy ($E = h\nu$) versus $(\alpha h\nu)^n$ where $n = 2$ and $1/2$ are used to fit the linear regions of the curve for direct and indirect transitions respectively. Extrapolation of the linear portion of the curve to the x-axis ordinate gives the energy of the band gap. The variation in optical band gap energy versus the mole percent of transition metal precursors in the delivery mixture for all dopants is shown in Fig. 1.

Cobalt doped pyrite ($\text{Co}_x\text{Fe}_{1-x}\text{S}_2$) thin films were deposited at 350°C by AACVD using precursors (1) and varying the concentration of (2). The evaluated direct energy band gaps are: 2.40 eV (0.05 mol%), 2.50 eV (0.10 mol%), 2.54 eV (0.15 mol%), 2.59 eV (0.20 mol%), 2.57 eV (0.25 mol%), and 2.40 eV (0.30 mol%). The evaluated indirect transitions are: 1.77 eV (0.05 mol%), 2.00 eV (0.10 mol%), 2.07 eV (0.15 mol%), 2.18 eV (0.20 mol%), 2.10 eV (0.25 mol%), and 1.85 eV (0.30 mol%) (Fig. S6, ESI†). The blue shift in optical absorption band edge of films suggests the formation of solid solution.³³ A similar behaviour has been noted by other laboratories.^{34,35}

The nickel doped pyrite ($\text{Ni}_x\text{Fe}_{1-x}\text{S}_2$) thin films were deposited at 350°C by AACVD using precursors (1) and varying the concentration of (3). The direct optical band gap (E_g) of nickel doped pyrite ($\text{Ni}_x\text{Fe}_{1-x}\text{S}_2$) thin films are: 2.40 eV (0.05 mol%), 2.10 eV (0.10 mol%), 2.12 eV (0.15 mol%), 2.40 eV (0.20 mol%), 1.97 eV (0.25 mol%), and 2.10 eV (0.30 mol%). The evaluated



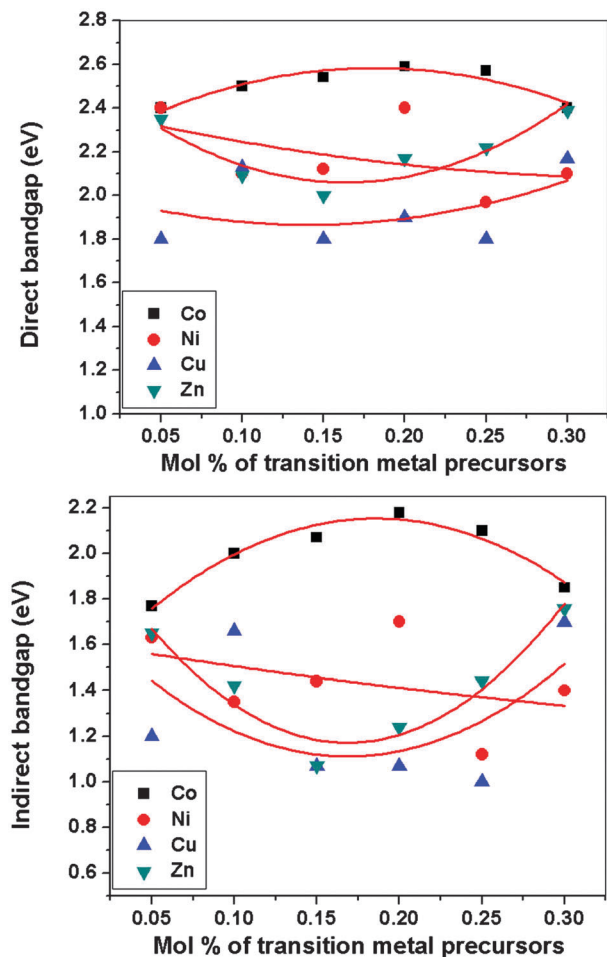


Fig. 1 Direct and indirect optical bandgaps vs. mol% of transition metal precursors for doped iron sulphide $M_x\text{Fe}_{1-x}\text{S}_2$ thin films (where $M = \text{Co}, \text{Ni}, \text{Cu}, \text{Zn}$) deposited at 350 °C on glass substrates synthesized by AACVD from complexes (1) in combination with (2), (3), (4) and (5).

indirect transitions are: 1.67 eV (0.05 mol%), 1.35 eV (0.10 mol%), 1.44 eV (0.15 mol%), 1.70 eV (0.20 mol%), 1.12 eV (0.25 mol%), and 1.40 eV (0.30 mol%) (Fig. S7, ESI†). The variation in band gap is linear with varying concentration of dopant precursor for $\text{Ni}_x\text{Fe}_{1-x}\text{S}_2$ thin films which indicates the gradual incorporation of nickel within pyrite. The blue shift in optical absorption band edge of films confirms the formation of solid solution.³⁶

The copper doped pyrite ($\text{Cu}_x\text{Fe}_{1-x}\text{S}_2$) thin films were deposited by AACVD at 350 °C using precursors (1) and varying the concentration of (4). The evaluated direct energy band gaps are: 1.80 eV (0.05 mol%), 2.13 eV (0.10 mol%), 1.80 eV (0.15 mol%), 1.90 eV (0.20 mol%), 1.80 eV (0.25 mol%), and 2.17 eV (0.30 mol%). The evaluated indirect transitions are: 1.20 eV (0.05 mol%), 1.66 eV (0.10 mol%), 1.07 eV (0.15 mol%), 1.07 eV (0.20 mol%), 1.00 eV (0.25 mol%), and 1.70 eV (0.30 mol%) (Fig. S8, ESI†). The blue shift in optical absorption band edge of films shows formation of solid solution.³⁷ The band gap varies in $\text{Cu}_x\text{Fe}_{1-x}\text{S}_2$ thin films with concentration of the dopant precursor but less than cobalt due to limited solubility.¹⁹

The zinc doped pyrite ($\text{Zn}_x\text{Fe}_{1-x}\text{S}_2$) thin films were deposited by AACVD at 350 °C using precursors (1) and varying the concentration of (5). The evaluated direct energy band gaps are: 2.35 eV (0.05 mol%), 2.09 eV (0.10 mol%), 2.00 eV (0.15 mol%), 2.17 eV (0.20 mol%), 2.22 eV (0.25 mol%), and 2.39 eV (0.30 mol%). The evaluated indirect transitions are: 1.65 eV (0.05 mol%), 1.42 eV (0.10 mol%), 1.07 eV (0.15 mol%), 1.24 eV (0.20 mol%), 1.44 eV (0.25 mol%), and 1.76 eV (0.30 mol%) (Fig. S9, ESI†). The blue shift in optical absorption band edge of films shows formation of solid solution. The enhancement in band gap of $\text{Zn}_x\text{Fe}_{1-x}\text{S}_2$ thin films is supported by previous observations.³⁸ Alloying pyrite with different elements involves issues like differences in electronegativity, size, band gap bowing and miscibility.¹⁹ Band gap bowing effect was observed in $\text{Fe}_x\text{M}_{1-x}\text{S}_2$ thin films. Increment in the band gap of $\text{Fe}_x\text{M}_{1-x}\text{S}_2$ thin films was observed, which might be attributed to transition metal doping, oxygen alloying and quantum confinement effects.¹⁸ Recently, first principle calculations investigated by Xiao *et al.* explored that biaxial strain can also increase band gap of pyrite.³⁹

3.2. Photoluminescence of doped pyrite films

Photoluminescence (PL) emission spectroscopy can probe band gap energy, impurities and defects within films, and surface structure. Radiative PL emission originates from exciton recombination, where an excited electron recombines with a hole, releasing a photon in the process. High PL quantum yields indicate higher recombination rate of the electron-hole pairs and the lifetime of the photoluminescent state is short.⁴⁰ Steady state PL measurements for transition metal doped pyrite ($\text{M}_x\text{Fe}_{1-x}\text{S}_2$) thin films deposited on glass substrates at 350 °C by AACVD was performed at an excitation wave length of 375 nm at ambient temperature.

The PL spectra of the cobalt doped pyrite ($\text{Co}_x\text{Fe}_{1-x}\text{S}_2$) thin films deposited at 350 °C using precursors (1) and varying the concentration of (2) (0.05 mol%, 0.1 mol%, 0.15 mol%, 0.20 mol%, 0.25 mol%, 0.30 mol%) show broad emission peaks in the range of 400–600 nm at different dopant concentration (Fig. S10, ESI†). The emission peaks strongly support band-to-band transitions, which occurs due to exciton recombination of the excited electron in the conduction band with a hole in the valence band. Small features between 550–675 nm are attributed to excitonic peaks in sample at dopant concentration of 0.05 mol%.

Nickel doped pyrite ($\text{Ni}_x\text{Fe}_{1-x}\text{S}_2$) thin films deposited at 350 °C using precursors (1) and varying concentration of (3) (0.00 mol%, 0.05 mol%, 0.1 mol%, 0.15 mol%, 0.20 mol%, 0.25 mol%, 0.30 mol%) show broad emission peaks between 389–400 nm for all samples (Fig. S11, ESI†). Small peaks at 500–700 nm might be attributed to the excitonic peaks due to defect states in sample at dopant concentration of 0.15 mol%. PL peak intensity decreases with the increase in nickel doping concentration corresponding to low recombination rates at higher nickel impurity level.

Copper doped pyrite ($\text{Cu}_x\text{Fe}_{1-x}\text{S}_2$) thin films deposited at 350 °C using precursors (1) and varying concentration of (4) (0.05 mol%, 0.1 mol%, 0.15 mol%, 0.20 mol%, 0.25 mol%, 0.30 mol%)



show broad emission peaks in the range of 390–400 nm (Fig. S12, ESI†). The zinc doped pyrite ($\text{Zn}_x\text{Fe}_{1-x}\text{S}_2$) thin films deposited at 350 °C using precursors (1) and varying concentration of (5) (0.05 mol%, 0.1 mol%, 0.15 mol%, 0.20 mol%, 0.25 mol%, 0.30 mol%) showed broad emission peaks in the range of 400–415 nm Fig. S13, ESI†). A similar behaviour was observed in pyrite composites or heterostructures.^{2,17}

3.3. Structural studies

Microstrain and dislocations in the crystal lattice of FeS_2 can have an influence upon the band gap of the material. Analysis of peak shifts or peak broadening in the powder X-ray diffraction (p-XRD) patterns of doped pyrite provides a quantification of lattice strain that is a measure of change in lattice constants attributable to crystal imperfections, such as dislocation. Strain may also emerge from crystallite size reduction and alloying.⁴¹ The average lattice constant can also be determined from interplanar spacing d_{hkl} :

$$\frac{1}{d_{hkl}} = \frac{a}{\sqrt{h^2 + k^2 + l^2}} \quad (1)$$

The lattice distortion degree can be expressed as:

$$\delta = \frac{a - a_0}{a_0} \quad (2)$$

where a_0 is the lattice constant of undoped pyrite (0.5420 nm) and a is the lattice constant of transition metal doped pyrite thin films under consideration.

The effect of lattice strain on diffraction peak position varies from peak shifting (uniform strain) to peak broadening (non-uniform strain). A change in the interplanar spacing (Δd) shifts the diffraction peaks toward lower or higher angle resulting a change in the Bragg angle ($\Delta\theta$). Lattice strain can be expressed as:

$$\frac{\Delta d}{d_0} = -\cot\theta\Delta\theta \quad (3)$$

where d_0 is the unstrained interplanar spacing; here it is referred as interplanar spacing for pyrite cubic structure ($\text{FeS}_{1.96}$ (ICDD No. 01-073-8127)). Microstrain (ε) is a very common physical phenomenon in nanocrystalline materials and thin films, and is defined as the strain that induces a deformation of one part per million and in thin films is often caused by crystal imperfections, point defects (vacancies, site disorder) and dislocations. The micro-strain (ε) and crystallite size (D) are interrelated by the Williamson–Hall equation:

$$B\cos\theta = \frac{k\lambda}{D} + 4\varepsilon\sin\theta \quad (4)$$

where k is the shape factor usually taken as 0.9 for spherical crystallites, λ is the X-ray wavelength and B is the full width at half-maximum (FWHM) of the peak under consideration. The Williamson–Hall equation partially originates from the Debye–Scherrer equation:

$$D = \frac{0.9\lambda}{B\cos\theta_B} \quad (5)$$

And thus micro-strain,⁴² can be expressed as follows:

$$\varepsilon = \frac{B}{4\tan\theta} \quad (6)$$

Conversely, dislocation density (δ) is related to crystallite size (D) by equation:⁴³

$$\delta = \frac{n}{D^2} \quad (7)$$

where n is a factor, which is almost equal to unity for minimum dislocation density. In this work, a typical calculation method has been applied using eqn (1), (6) and (7) (ref. 43).

p-XRD analysis of $\text{M}_x\text{Fe}_{1-x}\text{S}_2$ thin films deposited at 350 °C reveals that the diffraction peaks shift gradually towards lower 2θ values as compared to pyrite with preferred orientation along the (200) plane.³² The doping induces the lattice strain in $\text{M}_x\text{Fe}_{1-x}\text{S}_2$ thin films. The lattice parameter for the cubic doped films increases monotonically with doping and consequently induces microstrain in cubic structure of pyrite. The average value of microstrain was found to be least in the copper doped while the most in zinc doped pyrite thin films (Table 1). For all doped films, the microstrain values are higher than undoped FeS_2 (3.031×10^{-3}) which is caused by cation substitution that is in good agreement to previously reported values 3.4×10^{-3} to 3.4×10^{-4} for pyrite thin films calculated by Rietveld refinements of X-ray diffraction data.⁴⁴ Lattice distortion is caused by the difference in sizes the two metal ions into the pyrite lattice. Specifically, the microstrain caused by transition metal doping is proportional to dislocation density. Undoped pyrite thin films on glass substrates, which have a dislocation density of $1.075 \times 10^{-3} \text{ nm}^{-2}$ calculated by using eqn (7).

Divalent cations with ionic radius larger than Fe^{2+} incorporated into the FeS_2 structure form substitutional solid solutions and the lattice parameter should be increased. The lattice parameter ' a ' of films was calculated using eqn (2) as; 0.5420 nm for undoped FeS_2 and 0.5419–0.5444 nm ($\text{Co}_x\text{Fe}_{1-x}\text{S}_2$), 0.5422–0.5427 nm ($\text{Ni}_x\text{Fe}_{1-x}\text{S}_2$), 0.5428–0.5435 nm ($\text{Cu}_x\text{Fe}_{1-x}\text{S}_2$) and 0.5421–0.5422 nm ($\text{Zn}_x\text{Fe}_{1-x}\text{S}_2$). The increase of the lattice parameter suggests an increase of the interplanar crystal spacing. The average lattice distortion degree was found to be greatest in copper-doped pyrite thin films greater than the values already reported for pyrite thin films where $\delta < 0$.⁴⁵ The average value of dislocation density was found to be maximum in zinc doped and minimum in copper doped pyrite thin films. The most pronounced structural changes observed with p-XRD was observed in the case of copper-doped pyrite thin films where the lattice changes from cubic (pyrite-ICDD No. 01-073-8127) to tetragonal (chalcopyrite-ICDD No. 01-083-0984) denoted by star in Table 1 as-evidenced by the appearance of a peak at $2\theta = 29.5^\circ$. This deviation in structural parameters varies from cobalt to zinc doped pyrite thin films. The preferred orientation was along the (200) crystal plane for all dopants except copper doped pyrite thin films where phase transformation from pyrite to chalcopyrite at $x = 0.30$ mol% develops preferred orientation along the (112) plane. Some diffraction peaks were too weak to be observed at higher concentration of zinc precursor ($x = 0.30$ mol%) and pattern was observed as for amorphous material.³²



Table 1 Lattice constant, microstrain and dislocation density in $M_x\text{Fe}_{1-x}\text{S}_2$ ($x = 0.05$ to 0.3 mol%) thin films on glass substrates calculated using eqn (1), (6) and (7). Lattice constant ($a_0 = 0.5420$ nm), microstrain ($\epsilon_0 = 3.031 \times 10^{-3}$) and dislocation density ($\delta_0 = 1.075 \times 10^{-3} \text{ nm}^{-2}$) as calculated by using eqn (1), (6) and (7) in undoped FeS_2 thin films

| | x | $\text{Co}_x\text{Fe}_{1-x}\text{S}_2$ | $\text{Ni}_x\text{Fe}_{1-x}\text{S}_2$ | $\text{Cu}_x\text{Fe}_{1-x}\text{S}_2$ | $\text{Zn}_x\text{Fe}_{1-x}\text{S}_2$ |
|---|------|--|--|--|--|
| Lattice constant, (a , nm) | 0.05 | 0.5419 | 0.5425 | 0.5428 | 0.5421 |
| | 0.10 | 0.5422 | 0.5427 | 0.5434 | 0.5422 |
| | 0.15 | 0.5424 | 0.5422 | 0.5430 | 0.5421 |
| | 0.20 | 0.5425 | 0.5424 | 0.5432 | 0.5422 |
| | 0.25 | 0.5430 | 0.5426 | 0.5435 | 0.5421 |
| | 0.30 | 0.5444 | 0.5425 | 0.4177 ^a | Amorphous |
| Microstrain, (ϵ) $\times 10^{-3}$ | 0.05 | 3.147 | 3.542 | 3.606 | 4.179 |
| | 0.10 | 3.588 | 4.730 | 3.335 | 3.391 |
| | 0.15 | 2.508 | 3.032 | 2.995 | 3.852 |
| | 0.20 | 2.992 | 2.577 | 3.056 | 4.817 |
| | 0.25 | 3.633 | 2.756 | 2.982 | 3.866 |
| | 0.30 | 4.125 | 3.991 | 3.372 | Amorphous |
| Dislocation density, (δ , nm^{-2}) $\times 10^{-3}$ | 0.05 | 1.404 | 1.280 | 1.416 | 1.819 |
| | 0.10 | 2.770 | 3.158 | 1.063 | 1.295 |
| | 0.15 | 0.667 | 0.088 | 1.252 | 1.682 |
| | 0.20 | 0.080 | 0.082 | 1.048 | 2.083 |
| | 0.25 | 1.263 | 1.120 | 1.786 | 1.584 |
| | 0.30 | 1.799 | 2.557 | 1.190 | Amorphous |

^a Phase transformation from cubic pyrite to tetragonal chalcopyrite.

The $M_x\text{Fe}_{1-x}\text{S}_2$ films deposited by AACVD at 350°C on indium tin oxide (ITO) substrates were characterized by p-XRD. X-ray patterns of the as-deposited films (Fig. 2) show the cubic pyrite ($\text{FeS}_{1.96}$ (ICDD No. 01-073-8127)) phase. It was possible to index the Bragg reflections to the (111), (200), (210), (220), (311), (222), (023) and (321). The Bragg reflections at $2\theta = 30.273^\circ$ and 35.165° correspond to the (222) and (400) planes respectively for indium tin oxide (ITO) (ICDD ref No. 00-039-1058). The lattice mismatch of doped pyrite thin films from wide bandgap semiconductor and solar substrate indium tin oxide (ITO) was also investigated. Microstrain and dislocation density has a greater value for all the as-deposited $M_x\text{Fe}_{1-x}\text{S}_2$ thin films fabricated by AACVD at 350°C on indium tin oxide (ITO) substrates as

compared to glass substrates due to lattice imperfections originating from lattice misfit in the films (Table 2).⁴⁶ This behaviour is potentially related to small crystallite size on this substrate.⁴⁴

Unlike the conventional deposition methods, deposition of undoped and doped pyrite thin films using the solution-based process like aerosol assisted chemical vapour deposition (AACVD) requires the particular molarity of precursor solutions. Additionally, it is challenging to sustain the pyrite phase at the same time while varying dopants under similar experimental conditions. In general, we observed that diethyldithiocarbamate transition metal complexes produced good quality transition metal doped pyrite thin films.

The as-deposited $M_x\text{Fe}_{1-x}\text{S}_2$ thin films on the ITO substrate were further characterized by Raman spectroscopy which revealed that the pyrite phase is dominant in all films. The Raman spectrum of $\text{Co}_x\text{Fe}_{1-x}\text{S}_2$ ($x = 0.10$ mol%) thin films synthesised by AACVD at 350°C on indium tin oxide (ITO) substrates (Fig. 3(a)) shows three peaks at 341 , 375 , and 426 cm^{-1} , which are the characteristic active modes for pyrite (FeS_2) corresponding to the S_2 dumb bell libration (E_g), S-S in-phase stretch (A_g), and coupled libration and stretch (T_g) modes, respectively.⁵ We tentatively assign the Raman band at 320 cm^{-1} to minor marcasite impurities.⁴⁷⁻⁴⁹ The Raman spectrum of $\text{Ni}_x\text{Fe}_{1-x}\text{S}_2$ ($x = 0.10$ mol%) thin films synthesised by AACVD at 350°C on indium tin oxide (ITO) substrates (Fig. 3(b)) shows three peaks at 339 , 375 , and 410 cm^{-1} corresponding to characteristic active

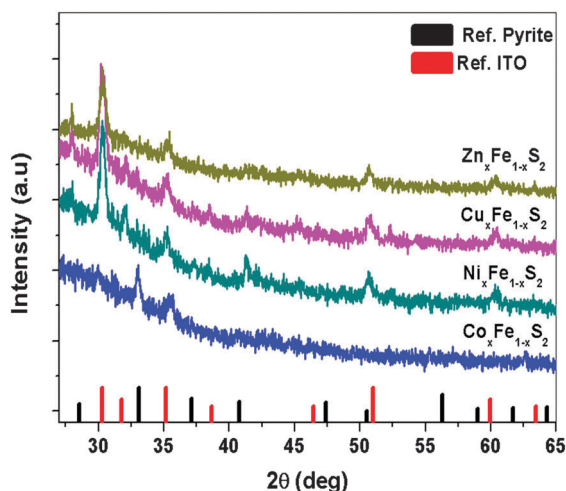


Fig. 2 p-XRD patterns of reference iron sulfide (pyrite- (ICDD No.01-073-8127)), indium tin oxide (ITO- (ICDD ref No. 00-039-1058)) and transition metal doped pyrite $M_x\text{Fe}_{1-x}\text{S}_2$ thin films at $x = 0.10$ mol% deposited from complexes (1) and (2), (3), (4) and (5) at 350°C on ITO substrates by AACVD.

Table 2 Microstrain and dislocation density in $M_x\text{Fe}_{1-x}\text{S}_2$ for $x = 0.10$ mol% thin films on ITO substrates calculated using eqn (5) and (6)

| $\times 10^{-3}$ | $\text{Co}_x\text{Fe}_{1-x}\text{S}_2$ | $\text{Ni}_x\text{Fe}_{1-x}\text{S}_2$ | $\text{Cu}_x\text{Fe}_{1-x}\text{S}_2$ | $\text{Zn}_x\text{Fe}_{1-x}\text{S}_2$ |
|---|--|--|--|--|
| Microstrain (ϵ) | 6.323 | 4.202 | 4.988 | 4.279 |
| Dislocation density (δ , nm^{-2}) | 3.395 | 2.100 | 2.371 | 2.085 |



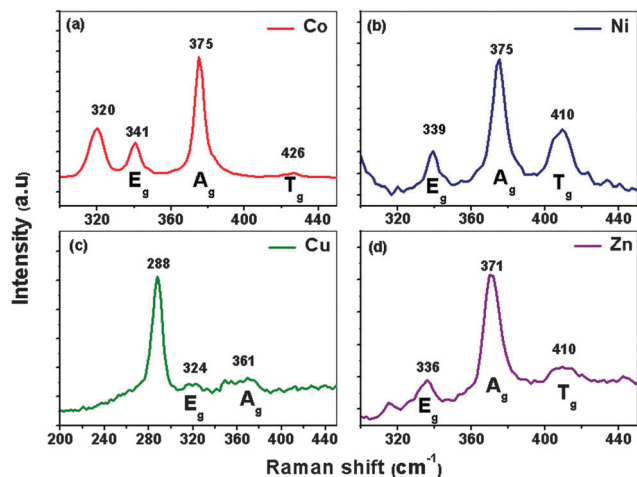


Fig. 3 Raman spectra of transition metal doped pyrite $M_xFe_{1-x}S_2$ thin films at $x = 0.10$ mol% deposited from complexes (1) and (2), (3), (4) and (5) at 350°C on ITO substrate deposited by AACVD.

modes for pyrite (FeS_2). $Ni_xFe_{1-x}S_2$ film shows no Raman band for substrate or marcasite impurity. The Raman spectrum of $Cu_xFe_{1-x}S_2$ ($x = 0.10$ mol%) thin films synthesised by AACVD at 350°C on indium tin oxide (ITO) substrates (Fig. 3(c)) exhibits three peaks at 288, 324, and 361 cm^{-1} corresponding to characteristic active modes for oxidized pyrite that might be due to long exposure time for film under high energy laser beam for ~ 1 min during spectrum capture. The chalcopyrite ($CuFeS_2$) structure exhibits bands at 287, 351 and 470 cm^{-1} .⁴⁷ Raman spectrum of films on ITO substrate have the expected vibrational modes at 109, 135, 307, 366, 495, 517 and 630 cm^{-1} assigned to In_2O_3 . The vibrational band at 631 cm^{-1} in the ITO spectrum is assigned to the contribution of the In–O (vibrational band at 630 cm^{-1}) and the Sn–O (vibrational modes at 633 cm^{-1}). The Sn–O exhibits vibrational modes at 144, 175, 240, 248, 433, 476 and 584 cm^{-1} .⁵⁰ The Raman spectrum of $Zn_xFe_{1-x}S_2$ ($x = 0.10$ mol%) thin films deposited at 350°C on indium tin oxide (ITO) substrates (Fig. 3(d)) displays three peaks at 336, 371, and 410 cm^{-1} corresponding to characteristic active modes for pyrite (FeS_2). $Zn_xFe_{1-x}S_2$ film shows no Raman band for the substrate or any marcasite impurities.

These observations demonstrate that all transition metal doped pyrite thin films $M_xFe_{1-x}S_2$ are cubic for all dopants except copper. This observation might be related to the miscibility of the respective sulfide of the transition metal complex at specific deposition temperature and dopant concentration conditions. Consequently, cation substitution in pyrite causes structural transformation and lattice strain.⁵¹ Also, extended laser irradiation (> 500 s) in air induces the substitution of sulfur by oxygen in the chalcogenide materials and the subsequent formation of transition metal oxides during Raman measurement.

3.4. Surface properties

The as-deposited transition metal doped pyrite ($M_xFe_{1-x}S_2$) thin films were characterized using atomic force microscopy (AFM) to explore their surface topography and morphology. Selective $M_xFe_{1-x}S_2$ thin films deposited on glass substrates at

350°C by AACVD using precursors (1) and varying concentration of the dopant precursors of (2–5) were imaged by AFM (Fig. 4). The morphology of $M_xFe_{1-x}S_2$ thin films depends on dopant concentration as well as on transition metal complex that is used as single source precursor. Overall surface morphology of thin films shows adherent, compact and crack/fracture free surfaces. Adherence is a chemical-physical phenomenon depending on the method of thin film fabrication and the adhesion at nanoscale decreases with increasing surface roughness.⁵² Thin films fabricated by chemical vapour deposition method are typically adherent. Average roughness values for $M_xFe_{1-x}S_2$ thin films varied as 13.9 nm, 7.9 nm, 6.8 nm and 6.1 nm. Variation in crystallite size and growth with doping has been discussed previously.³²

Surface analysis of transition metal doped pyrite ($M_xFe_{1-x}S_2$) thin films confirms the presence of uniform and crack-free surfaces. Thin film crystalline quality, morphology and texture are associated with surface roughness. The surface roughness in transition metal (Co, Ni, Cu, Zn) doped pyrite ($M_xFe_{1-x}S_2$) thin films deviate with dopant concentration and transition metal precursors. Zinc doped pyrite thin films showed the smoothest surfaces. Particle roughness and height profiles were studied using atomic force microscopy (AFM). Fig. 4 shows that the surface texture of the films varies from granular to the spherical growth of the particles in thin films with varying concentration of dopant. Moreover, roughness parameters, skewness (R_{sk}) and kurtosis (R_{ku}) were calculated from AFM analysis. Positive low values of skewness ($R_{sk} = 0.396, 0.0843, 0.089, 0.404$) display that peaks are somewhat dominant on the films surface while the kurtosis values ($R_{ku} = 3.578, 3.307, 2.524, 2.301$) indicate that the grain distribution over the scanned area has comparatively few high peaks and low valleys which indicates a slightly undulating surface.⁵³ Surface morphology plays an important role in photovoltaic devices.⁵⁴ AFM height profiles of transition metal doped

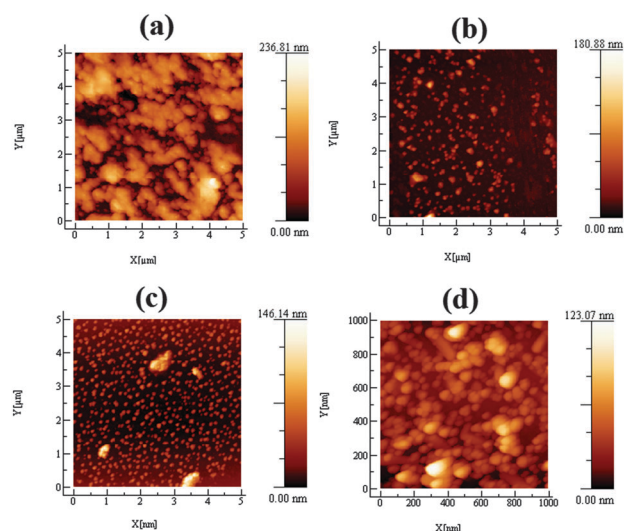


Fig. 4 Height-profile AFM images of transition metal doped pyrite ($M_xFe_{1-x}S_2$) thin films deposited at 350°C on glass substrates by AACVD from complexes (a) (1) and (2) at $x = 0.05$ mol%, (b) (1) and (4) at $x = 0.30$ mol%, (c and d) (1) and (5) at $x = 0.30$ mol%.



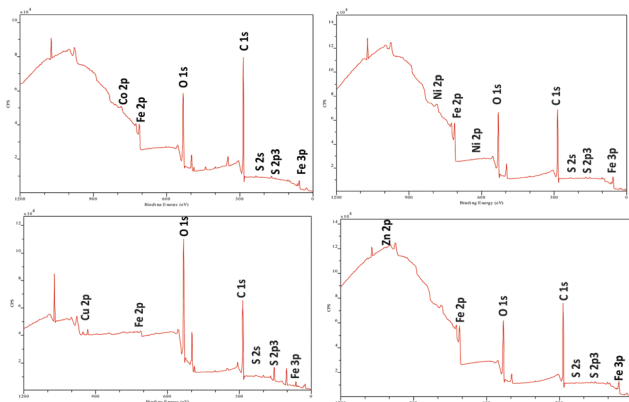


Fig. 5 XPS spectra of transition metal doped pyrite $M_xFe_{1-x}S_2$ thin films at $x = 0.30$ mol% deposited from complexes (1) and (2), (3), (4) and (5) at 350 °C on glass substrate deposited by AACVD.

pyrite ($M_xFe_{1-x}S_2$) thin films show uniform distribution of particles with average particle height 130 nm (Fig. 4). AFM data for scanning areas ranging from 0.5×0.5 up to $1 \times 1 \mu m^2$ for transition metal doped pyrite films revealed smooth surfaces having root mean squared (RMS) roughness values of 18.9 nm, 10.0 nm, 8.3 nm and 7.4 nm (Fig. 4). These smooth films doped with cobalt show microstrain values similar to FeS_2 itself and suggests that microstrain may be correlated to the overall smoothness of films grown by AACVD.⁵⁵

Photoelectron spectroscopy (XPS) was used for qualitative analysis of selected transition metal doped pyrite ($M_xFe_{1-x}S_2$) thin films prepared by AACVD using precursors (1) and the dopant precursors (2-5) of concentration 0.30 mol%. Integration and comparison of the Fe 2p, Co 2p, Ni 2p, Cu 2p and Zn 2p signals revealed compositions of transition metal doped pyrite thin films ($M_xFe_{1-x}S_2$). XPS analysis (Fig. 5) revealed phase transformation of pyrite to doped pyrite with an approximate surface composition of $M_xFe_{1-x}S_2$ (discounting other inconsequential species that may be present).⁵⁶⁻⁵⁸ Copper doped pyrite thin film at $x = 0.30$ mol% revealed transformation from pyrite (FeS_2) to chalcopyrite ($CuFeS_2$) at binding energy 161.3 eV of S 2p_{3/2} and 74.65 eV for Cu 3p_{3/2} (Fig. 5).

Density functional theory (DFT) calculation revealed that the interaction of impure pyrite (impurities like As, Co and Ni) with oxygen can enhance the oxidation of pyrite.⁵⁹ Pyrite containing impurities observed to be more reactive than un-doped pyrite.^{60,61} XPS studies of the oxidized transition metal doped pyrite revealed the shifting of binding energies of surface components towards higher binding energies as compared to pure pyrite.⁵⁶ This observation is in accordance with the results from XPS studies suggesting that bulk defect states introduced in doped pyrite increase the density of occupied surface states which mediate charge transfer and thus oxidation.⁶²

Thus, surface study reveals the influence of doping on oxidation processes related to the surface defects.

Subsequently, pyrite cannot simply be compared with and developed along the line of classical semiconductor compounds. Some structural parameters were qualitatively discussed in the

present work, but categorically, further systematic work is required to establish the role of impurities in doped pyrite to improve its properties.

4. Conclusions

Despite their promise, photovoltaic modules containing FeS_2 continue to show small photovoltages which have limited power conversion efficiencies to around 3%. Bandgap engineering of pyrite by doping may help in increasing power conversion efficiency by increasing the portion of the solar spectrum absorbed. Transition metal doped iron pyrite ($M_xFe_{1-x}S_2$) thin films were deposited on glass and indium tin oxide (ITO) coated glass substrates by AACVD using diethyldithiocarbamate complexes of the general formula $[M(S_2CN(Et)_2)_n]$. Lattice parameters and optical band gap confirmed the formation of a solid solution as determined by powder X-ray diffraction (p-XRD) and UV-Vis spectroscopy. Raman spectroscopy also helped to identify the phase of films deposited on ITO substrates. Atomic force microscopy (AFM) confirmed crack free surfaces. X-ray photoelectron spectroscopy (XPS) allowed the evaluation of species at the surface $M_xFe_{1-x}S_2$ thin films.

The structural properties of the transition metal doped pyrite ($M_xFe_{1-x}S_2$) depend strongly on the transition metal dopant used. Preferred orientation in all $M_xFe_{1-x}S_2$ thin films was observed to be along (200) plane. The influence of transition metal doping on the structure and phase transformation was significant in copper doped pyrite thin films. Optical studies revealed that there is increment in the bandgap of $M_xFe_{1-x}S_2$ thin films which is supported by previous work. There may be contribution from oxidation of the doped pyrite surface in band gap enhancement. Most of theoretical studies regarding band gap enhancement of doped pyrite propose that transition metals (Ni, Cu) introduce new defect states within pyrite structure.⁵¹ Density functional theory (DFT) calculations show that oxygen alloying in pyrite can increase its band gap 1.0–1.5 eV without introducing electronic states within the bandgap.¹⁸ There may be contribution in band gap enhancement from oxygen alloying. Similar results have been reported previously.⁶³

Lattice parameter increases can be correlated with the quantity of the dopant transition metal ion incorporated. The band gap of the $M_xFe_{1-x}S_2$ thin films increases with increasing dopant in all cases. Previously, improved photoresponse was observed with zinc alloyed into the $Zn_xFe_{1-x}S_2$ nanocrystal photoconductor attributed to the increased band gap.³⁸ Improved optical absorption with transition metal doping was observed in the $M_xFe_{1-x}S_2$ thin films engineering the optical bandgap. These may open the opportunities for photovoltaic applications using the $M_xFe_{1-x}S_2$ thin films with engineered wider bandgaps than pyrite.

Acknowledgements

SK thanks the Higher Education Commission of Pakistan for an IRSIP scholarship and the POB group (The University of Manchester, United Kingdom) for assistance with this research. SK is also grateful to Nano Science and Catalysis Division (NS&CD),



National Centre for Physics (NCP) Islamabad, Pakistan for providing research facilities as hosted researcher. This work was also funded by the UK Engineering and Physical Sciences Research Council (EPSRC) Core Capability in Chemistry grant (EPSRC grant number EP/K039547/1). We thank Dr John Walton (University of Manchester) for performing XPS measurements and Dr Louise Natrajan (University of Manchester) for access to the spectrofluorimeter.

References

- 1 C. Wadia, A. P. Alivisatos and D. M. Kammen, *Environ. Sci. Technol.*, 2009, **43**, 2072–2077.
- 2 M. A. Khan, J. Sarker, S. Lee, S. C. Mangham and M. Manasreh, *Mater. Chem. Phys.*, 2014, **148**, 1022–1028.
- 3 M. Wang, C. Xing, K. Cao, L. Zhang, J. Liu and L. Meng, *J. Mater. Chem. A*, 2014, **2**, 9496–9505.
- 4 X. Wen, X. Wei, L. Yang and P. K. Shen, *J. Mater. Chem. A*, 2015, **3**, 2090–2096.
- 5 M. S. Faber, M. A. Lukowski, Q. Ding, N. S. Kaiser and S. Jin, *J. Phys. Chem. C*, 2014, **118**, 21347–21356.
- 6 G. Srivastava, C. K. Das, A. Das, S. K. Singh, M. Roy, H. Kim, N. Sethy, A. Kumar, R. K. Sharma, S. K. Singh, D. Philip and M. Das, *RSC Adv.*, 2014, **4**, 58495–58504.
- 7 Y. Bai, J. Yeom, M. Yang, S.-H. Cha, K. Sun and N. A. Kotov, *J. Phys. Chem. C*, 2013, **117**, 2567–2573.
- 8 M. Zhang, B. Chen, H. Tang, G. Tang, C. Li, L. Chen, H. Zhang and Q. Zhang, *RSC Adv.*, 2015, **5**, 1417–1423.
- 9 H. J. Snaith, *J. Phys. Chem. Lett.*, 2013, **4**, 3623–3630.
- 10 A. Chirilă, S. Buecheler, F. Pianezzi, P. Bloesch, C. Gretener, A. R. Uhl, C. Fella, L. Kranz, J. Perrenoud, S. Seyrling, R. Verma, S. Nishiwaki, Y. E. Romanyuk, G. Bilger and A. N. Tiwari, *Nat. Mater.*, 2011, **10**, 857–861.
- 11 D. J. Lewis, P. Kevin, O. Bakr, C. A. Muryn, M. A. Malik and P. O'Brien, *Inorg. Chem. Front.*, 2014, **1**, 577–598.
- 12 D. J. Binks, *Phys. Chem. Chem. Phys.*, 2011, **13**, 12693–12704.
- 13 S. N. Malik, S. Mahboob, N. Haider, M. A. Malik and P. O'Brien, *Nanoscale*, 2011, **3**, 5132–5139.
- 14 S. N. Malik, A. Q. Malik, R. F. Mehmood, G. Murtaza, Y. G. Alghamdi and M. A. Malik, *New J. Chem.*, 2015, **39**, 4047–4054.
- 15 M. Azad Malik, N. Revaprasadu and K. Ramasamy, *Nanomaterials for solar energy, Nanoscience: Volume 1: Nanostructures through Chemistry*, The Royal Society of Chemistry, 2013, pp. 29–59.
- 16 P. Lazić, R. Armiento, F. Herbert, R. Chakraborty, R. Sun, M. Chan, K. Hartman, T. Buonassisi, B. Yildiz and G. Ceder, *J. Phys.: Condens. Matter*, 2013, **25**, 465801.
- 17 A. Kirkeminde, R. Scott and S. Ren, *Nanoscale*, 2012, **4**, 7649–7654.
- 18 J. Hu, Y. Zhang, M. Law and R. Wu, *J. Am. Chem. Soc.*, 2012, **134**, 13216–13219.
- 19 R. Sun and G. Ceder, *Phys. Rev. B: Condens. Matter Mater. Phys.*, 2011, **84**, 245211.
- 20 N. Revaprasadu, M. A. Malik, P. O'Brien and G. Wakefield, *J. Mater. Res.*, 1999, **14**, 3237–3240.
- 21 M. A. Malik, M. Motevalli and P. O'Brien, *Inorg. Chem.*, 1995, **34**, 6223–6225.
- 22 M. A. Malik, M. Motevalli, J. R. Walsh and P. O'Brien, *Organometallics*, 1992, **11**, 3136–3139.
- 23 A. A. Memon, M. Afzaal, M. A. Malik, C. Q. Nguyen, P. O'Brien and J. Raftery, *Dalton Trans.*, 2006, 4499–4505.
- 24 D. Binks, S. Bant, D. West, P. O'Brien and M. Malik, *J. Mod. Opt.*, 2003, **50**, 299–310.
- 25 C. Q. Nguyen, A. Adeogun, M. Afzaal, M. A. Malik and P. O'Brien, *Chem. Commun.*, 2006, 2182–2184.
- 26 M. A. Malik, M. Motevalli, T. Saeed and P. O'Brien, *Adv. Mater.*, 1993, **5**, 653–654; K. Ramasamy, M. A. Malik, N. Revaprasadu and P. O'Brien, *Chem. Mater.*, 2013, **25**, 3551–3569.
- 27 A. Panneerselvam, C. Q. Nguyen, M. A. Malik, P. O'Brien and J. Raftery, *J. Mater. Chem.*, 2009, **19**, 419–427.
- 28 D. J. Lewis and P. O'Brien, *Chem. Commun.*, 2014, **50**, 6319–6321.
- 29 P. Kevin, S. N. Malik, M. A. Malik and P. O'Brien, *Chem. Commun.*, 2014, **50**, 14328–14330.
- 30 P. Kevin, D. J. Lewis, J. Raftery, M. Azad Malik and P. O'Brien, *J. Cryst. Growth*, 2015, **415**, 93–99.
- 31 M. Akhtar, M. A. Malik, J. Raftery and P. O'Brien, *J. Mater. Chem. A*, 2014, **2**, 20612–20620.
- 32 S. Khalid, E. Ahmed, M. Azad Malik, D. J. Lewis, S. Abu Bakar, Y. Khan and P. O'Brien, *New J. Chem.*, 2015, **39**, 1013–1021.
- 33 Y. Tamm, R. Schieck, K. Ellmer and S. Fiechter, *J. Cryst. Growth*, 1995, **146**, 271–276.
- 34 J. Jiao, L. Chen, D. Kuang, W. Gao, H. Feng and J. Xia, *RSC Adv.*, 2011, **1**, 255–261.
- 35 F. Long, J. He, M. Zhang, X. Wu, S. Mo, Z. Zou and Y. Zhou, *J. Mater. Sci.*, 2015, **50**, 1848–1854.
- 36 R. Chandler and R. Bene, *Phys. Rev. B: Solid State*, 1973, **8**, 4979.
- 37 I. Ferrer, F. Caballero, C. De las Heras and C. Sánchez, *Solid State Commun.*, 1994, **89**, 349–352.
- 38 B. Mao, Q. Dong, Z. Xiao, C. L. Exstrom, S. A. Darveau, T. E. Webber, B. D. Lund, H. Huang, Z. Kang and J. Huang, *J. Mater. Chem. A*, 2013, **1**, 12060–12065.
- 39 P. Xiao, X.-L. Fan, L.-M. Liu and W.-M. Lau, *Phys. Chem. Chem. Phys.*, 2014, **16**, 24466–24472.
- 40 T. H. Gfroerer, *Encyclopedia of Analytical Chemistry*, 2000.
- 41 P. Scardi, M. Leoni and R. Delhez, *J. Appl. Crystallogr.*, 2004, **37**, 381–390.
- 42 V. Mote, Y. Purushotham and B. Dole, *J. Theor. Appl. Phys.*, 2012, **6**, 1–8.
- 43 P. Chelvanathan, Y. Yusoff, F. Haque, M. Akhtaruzzaman, M. Alam, Z. Alothman, M. Rashid, K. Sopian and N. Amin, *Appl. Surf. Sci.*, 2015, **334**, 138–144.
- 44 C. De las Heras, J. de Vidales, I. Ferrer and C. Sánchez, *J. Mater. Res.*, 1996, **11**, 211–220.
- 45 L. Y. Huang and L. Meng, *Mater. Sci. Eng., B*, 2007, **137**, 310–314.
- 46 L. Meng, Y. Liu and L. Tian, *J. Cryst. Growth*, 2003, **253**, 530–538.



- 47 S. N. White, *Chem. Geol.*, 2009, **259**, 240–252.
- 48 C. Sourisseau, R. Cavagnat and M. Fouassier, *J. Phys. Chem. Solids*, 1991, **52**, 537–544.
- 49 H. Lutz and B. Müller, *Phys. Chem. Miner.*, 1991, **18**, 265–268.
- 50 O. M. Berengue, A. D. Rodrigues, C. J. Dalmaschio, A. J. Lanfredi, E. R. Leite and A. J. Chiquito, *J. Phys. D: Appl. Phys.*, 2010, **43**, 045401.
- 51 P. Abraitis, R. Patrick and D. Vaughan, *Int. J. Miner. Process.*, 2004, **74**, 41–59.
- 52 R. De Oliveira, D. Albuquerque, F. Leite, F. Yamaji and T. Cruz, *Measurement of the nanoscale roughness by atomic force microscopy: basic principles and applications*, INTECH Open Access Publisher, 2012.
- 53 E. S. Gadelmawla, M. M. Koura, T. M. A. Maksoud, I. M. Elewa and H. H. Soliman, *J. Mater. Process. Technol.*, 2002, **123**, 133–145; R. Muhammad, A. M. Rana, M. Hafeez, E. Ahmed, A. S. Bhatti, M. F. Wasiq and M. Y. Nadeem, *Acta Chim. Slov.*, 2014, **61**, 80–86.
- 54 C. Teichert and I. Beinik, Conductive atomic-force microscopy investigation of nanostructures in microelectronics, *Scanning Probe Microscopy in Nanoscience and Nanotechnology*, 2011, vol. 2, pp. 691–721.
- 55 J.-G. Yoon, H. K. Oh and S. J. Lee, *Phys. Rev. B: Condens. Matter Mater. Phys.*, 1999, **60**, 2839.
- 56 S. Mattila, J. A. Leiro and K. Laajalehto, *Appl. Surf. Sci.*, 2003, **212–213**, 97–100.
- 57 S. Mattila, J. A. Leiro and M. Heinonen, *Surf. Sci.*, 2004, **566–568**(part 2), 1097–1101.
- 58 A. G. Schaufuß, H. W. Nesbitt, I. Kartio, K. Laajalehto, G. M. Bancroft and R. Szargan, *Surf. Sci.*, 1998, **411**, 321–328.
- 59 Y.-Q. Li, J.-H. Chen, Y. Chen and J. Guo, *Trans. Nonferrous Met. Soc. China*, 2011, **21**, 1887–1895.
- 60 S. Lehner, K. Savage, M. Ciobanu and D. E. Clifffel, *Geochim. Cosmochim. Acta*, 2007, **71**, 2491–2509.
- 61 S. Lehner and K. Savage, *Geochim. Cosmochim. Acta*, 2008, **72**, 1788–1800.
- 62 K. S. Savage, D. Stefan and S. W. Lehner, *Appl. Geochem.*, 2008, **23**, 103–120.
- 63 B. J. Richardson, L. Zhu and Q. Yu, *Sol. Energy Mater. Sol. Cells*, 2013, **116**, 252–261.

